

Article

Photocatalytic Degradation of Antibiotics by Superparamagnetic Iron Oxide Nanoparticles. Tetracycline Case

Sunday Joseph Olusegun, Gonzalo Larrea, Magdalena Osial , Krystyna Jackowska and Pawel Krysinski * 

Faculty of Chemistry, University of Warsaw, Pasteur Street 1, 02-093 Warsaw, Poland; o.sunday@chem.uw.edu.pl (S.J.O.); g.larrea@student.uw.edu.pl (G.L.); mosial@chem.uw.edu.pl (M.O.); kryjacko@chem.uw.edu.pl (K.J.)

* Correspondence: pakrys@chem.uw.edu.pl; Tel.: +48-225526412

Abstract: The challenges associated with the uncontrolled presence of antibiotics such as tetracycline in the environment have necessitated their removal through different techniques. Tetracycline is hard to degrade in living organisms and can even be converted to more toxic substances. In view of this, we synthesized iron oxide nanoparticles with good magnetization (70 emu g^{-1}) and 15 nm particle size for the adsorption and photocatalytic degradation of tetracycline. Characterization carried out on the synthesized iron oxides revealed a bandgap of 1.83 eV and an isoelectric point at pH 6.8. The results also showed that the pH of the solution does not directly influence the adsorption of tetracycline. The adsorption isotherm was consistent with the model proposed by Langmuir, having 97 mg g^{-1} adsorption capacity. Combined with the superparamagnetic behavior, this capacity is advantageous for the magnetic extraction of tetracycline from wastewater. The mechanisms of adsorption were proposed to be hydrogen bonding and $n-\pi$ interactions. Photocatalytic degradation studies showed that approximately 40% of tetracycline degraded within 60 min of irradiation time with UV/vis light. The kinetics of photodegradation of tetracycline followed the pseudo-first-order mechanism, proceeding through hydroxyl radicals generated under illumination. Moreover, the photogenerated hydrogen peroxide could lead to heterogeneous photo-Fenton processes on the surface of iron oxide nanoparticles, additionally generating hydroxyl and hydroperoxyl radicals and facilitating photodegradation of tetracycline.

Keywords: maghemite; tetracycline; adsorption; photocatalysis; mechanism; eco-friendly water treatment



Citation: Olusegun, S.J.; Larrea, G.; Osial, M.; Jackowska, K.; Krysinski, P. Photocatalytic Degradation of Antibiotics by Superparamagnetic Iron Oxide Nanoparticles. Tetracycline Case. *Catalysts* **2021**, *11*, 1243. <https://doi.org/10.3390/catal11101243>

Academic Editors: Juan García Rodríguez and Silvia Álvarez-Torrellas

Received: 18 September 2021
Accepted: 13 October 2021
Published: 15 October 2021

Publisher's Note: MDPI stays neutral with regard to jurisdictional claims in published maps and institutional affiliations.



Copyright: © 2021 by the authors. Licensee MDPI, Basel, Switzerland. This article is an open access article distributed under the terms and conditions of the Creative Commons Attribution (CC BY) license (<https://creativecommons.org/licenses/by/4.0/>).

1. Introduction

Antibiotics were developed to limit the mortality rate and boost human and animal immune systems which have been negatively affected by the invasion of different bacteria's infection. In livestock farming, it is used as food additives for the promotion of growth and inhibition of diseases [1,2]. Meanwhile, the uncontrolled disposal of antibiotics into the environment has compromised their disease-fighting ability and made them detrimental to human health. Antibiotics are discharged into the environment through industrial (pharmaceutical industries), hospital, household, and livestock wastewater [3]. Since only 30% of the antibiotics that humans and animals are taking are diffusing through the body system to fight diseases, the remaining 70% are defecated into the environment without being metabolized [4,5]. This has led to an increase in bacterial resistance to antibiotics and a lack of effectiveness of antibiotics in fighting against bacteria that are responsible for various diseases [6].

Among the classes of antibiotics that are widely used are tetracyclines. Under their classification, there is tetracycline (TC) itself. TC is widely used in many countries as human and animal medicine because it poses a great threat to disruption of microbial populations and is effective in treating diseases like trachoma, pneumonia, and acute diarrhea, among others [7,8]. It is cost affordable for many patients and farmers that use it

for their livestock [9] However, its by-products are hazardous to the ecosystem and among them are anhydrotetracycline and epitetraacycline hydrochloride which are recognized to be similarly toxic as the parent compound [10,11]. Therefore, it is necessary to eliminate it from the environment to prevent its toxicity on humans and animals and limit the increase in the number of bacteria that have developed resistance to TC's effectiveness [12].

One of the ways to reduce the toxicity and propagation of bacteria resistance to antibiotics is to treat wastewater that contains antibiotics adequately before discharging it into the environment. Therefore, different techniques had been developed and used to reduce the deadly impact of the inappropriate discharge of antibiotics into the environment. These include reverse osmosis, biological treatment, electrocoagulation, ion exchange, membrane filtration, degradation, among others [13–20]. Meanwhile, the chemical stability, structure, and non-biodegradable nature of TC have made its removal through the conventional waste-water treatment difficult [21]. More so, various shortcomings associated with the use of listed methods have resulted in advancement in the application of adsorption and photocatalysis as an alternative and efficient method to remove antibiotics from wastewater.

Adsorption is a surface phenomenon in which contaminants in the bulk solution concentrate on the surface of adsorbents without changing the structure of the adsorbed contaminants [22]. The photocatalysis technique on the other hand has enabled total mineralization of organic contaminants into CO_2 , H_2O , and mineral acids [8,23]. Both techniques are easy to set up, operate effectively at room temperature, cost-effective, and eco-friendly without leading to secondary pollutants [8,24]. The combination of these techniques was investigated for the removal of tetracycline hydrochloride using $\text{BiVO}_4/\text{MoO}_3$ [25]. According to the authors the combined processes favorably removed the targeted contaminants.

In recent time different materials have been used as either as adsorbents or photocatalysts for treatment of various contaminants, among which are Fe-based ceramic nanocomposite membranes that were fabricated through e-spinning and vacuum filtration, $\text{AgBr}/\text{h-MoO}_3$ among others [26,27]. The $\text{Fe}_2\text{O}_3\text{-CuO-MoO}_3$ magnetic composite has also been used as photocatalyst for the degradation of methylene blue [28].

However, an ideal adsorbent and photocatalyst should be nontoxic, inexpensive, stable, readily available, and highly photoactive (in the case of photocatalysis). Combining these two techniques will be helpful to enhance the effectiveness of materials in removing contaminants from the environment. Because of this, we prepared iron oxides nanoparticle for the adsorption and photocatalytic degradation of tetracycline. The kinetic of the removal process was studied and mechanisms of adsorption and photocatalytic degradation were proposed. Moreover, because of their superparamagnetic and photocatalytic properties, these nanoparticles are economically competitive to other nano adsorbents and nanocatalysts due to the opportunity for magnetic separation and further reuse in combined adsorption and photocatalytic treatment of wastewater. Additionally, superparamagnetic iron oxide nanoparticles can open up a new photocatalytic photo-Fenton degradation pathway of tetracycline, increasing their efficiency in wastewater decontamination. Therefore, the contribution of hydroxyl radicals and hydrogen peroxide reactive species was also identified experimentally.

2. Results and Discussion

2.1. Characterization of Maghemite Nanoparticles

The SEM morphology of the synthesized maghemite nanoparticles depicts the agglomeration of nanoparticles fused with the presence of cavities (pores) in between the bulk of agglomerates (Figure 1A). The TEM image in Figure 1B shows nanoparticles of uniform, well-defined, round shape with an average diameter of about 15 nm. Overlapping of nanoparticles (NPs), as shown in the image, is caused by a high concentration of NPs in the suspension and slow evaporation of aqueous solvent while drying. Figure 1C shows the magnetization of maghemite versus the applied magnetic field, performed at 300 K, having saturation magnetization of 70 emu g^{-1} . The result showed the absence of

remanence and almost zero coercivity, which is evidence of superparamagnetic behavior of maghemite nanoparticles [29] being sufficiently small to behave like single magnetic domains [30]. That is advantageous for application in wastewater treatment because the catalyst nanoparticles can be recovered from the system with the help of a magnet, cleaned, and subsequently reused for photocatalysis without additional dispersion processes after the magnetic field is removed.

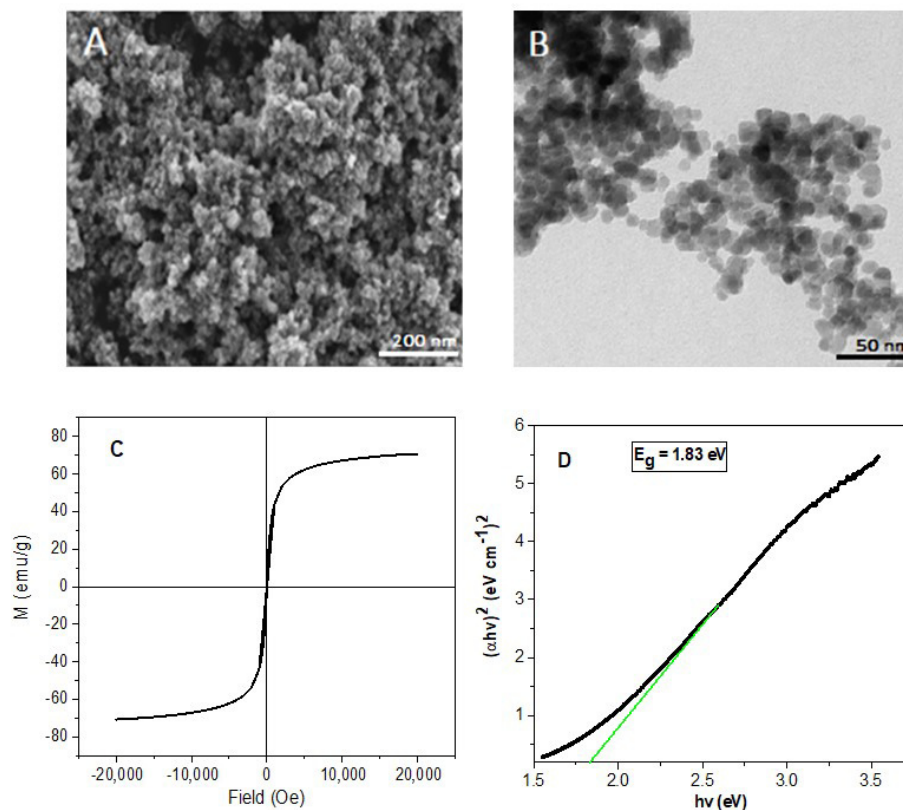


Figure 1. SEM (A) and TEM (B) images of maghemite nanoparticles, magnetization versus applied field (C), and the bandgap of maghemite nanoparticles (D).

The data obtained from UV–vis diffuse reflectance spectroscopy (DRS) for the optical absorbance of maghemite nanoparticles were used to calculate the band gap energy by using Tauc derived equation (Equation (1)).

$$\alpha(h\nu) = K(h\nu - E_g)^n \quad (1)$$

The parameters in this equation are defined as follows: α is the absorption coefficient, $h\nu$ is the photon energy, K is constant, E_g is the optical band gap energy, and n is the electronic transition (where $n = 2$ corresponds to an indirect bandgap, and $n = \frac{1}{2}$ stands for direct bandgap). As shown in Figure 1D, the band gap energy (E_g) of maghemite nanoparticles was obtained by extrapolating the linear part of the plot of $\alpha(h\nu)^2$ versus $h\nu$ to the X-axis. The value of the bandgap obtained is 1.83 eV. This is slightly lower than 2 eV that was extrapolated for maghemite synthesized by Rehman et al., [31], but higher than 0.5 eV that was obtained as magnetite band gap energy by Giannakis et al., [32]. Therefore, 1.83 eV that we extrapolated in our study may be due to the mixture of maghemite with a small addition of magnetite.

The powder X-ray diffraction patterns (PXRD) of as-obtained maghemite nanoparticles are shown in Figure 2. The position and intensities of the diffraction peaks were identified and compared with the DB card number 9002673 using Rietveld method. Thus, our

superparamagnetic nanoparticles crystallized in a reverse spinel (space group $Fd\bar{3}m$), characteristic for maghemite [33–36].

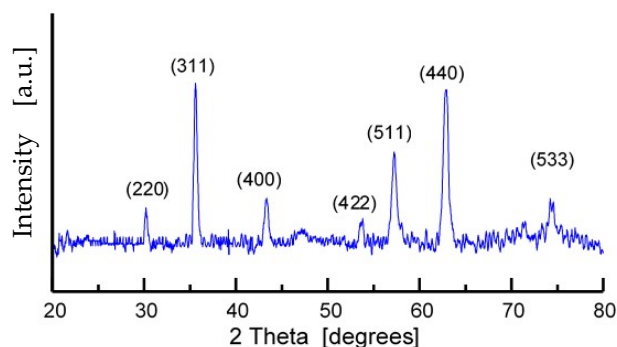


Figure 2. The PXRD diffraction pattern of as-prepared maghemite nanoparticles with the hkl indices characteristic for $Fd\bar{3}m$ space group.

2.2. pH Effect on the Adsorption of TC

The result, as presented in Figure 3A, is the amount (mg g^{-1}) of TC that was adsorbed between pH 2 to 10. The amount of adsorbed TC increased to pH 6 (where it reached the maximum) and later decreased at pH 8 and 10. The lowest amount (30 mg g^{-1}) was adsorbed at pH 2, while the highest amount (57 mg g^{-1}) was adsorbed at pH 6. This adsorption behavior can be understood in terms of the protonation and deprotonation state of TC at various pH, coupled with the surface charge of maghemite at various pH. According to literature, TC is in a fully protonated state (TCH_3^+) at $\text{pH} < 3$, zwitterionic (TCH_2) at $\text{pH} 3\text{--}7$, monoanionic (TCH^-) at $\text{pH} 7\text{--}9.7$, and double anionic state (TC^{2-}) at $\text{pH} > 10$ [37–39]. The information on the surface charge of maghemite that we obtained from the zeta potential measurements shows that its surface charge is positive at pH below 7, and negative at pH above 7 (Figure 3B). The isoelectric point (IEP) is at $\text{pH} 6.8$. This value is in agreement with the previous work of Boguslavsky and Margel, Watanabe and Seto [40,41]. In summary, it implies that Fe-O^- is predominant in the basic medium while Fe-OH^{2+} dominates in the acidic medium.

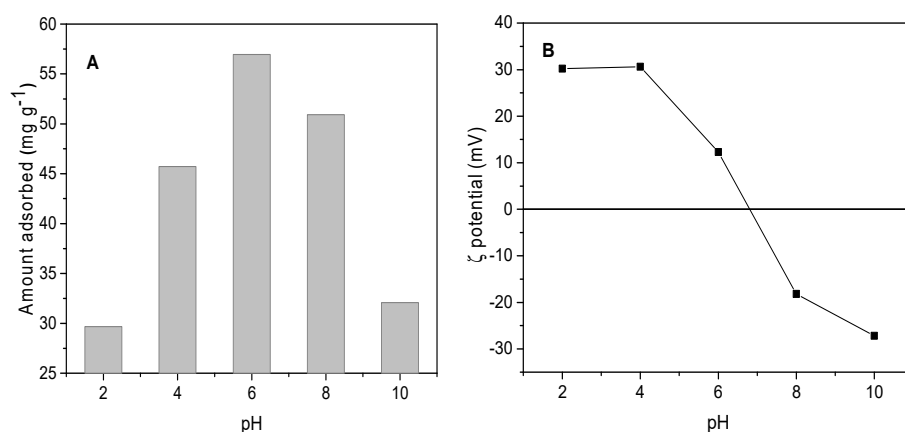


Figure 3. The amount of TC that was adsorbed versus solution pH (A), and the zeta potential measurement of maghemite (B).

Relating the ionization of TC and the surface charge of maghemite, one will expect electrostatic repulsion between the positively charged NP's surface and the TCH_3^+ (Protonated state of TC) at pH 2. Contrary to this, approximately 30 mg g^{-1} of TC was adsorbed. More so, at pH 6, where the maximum amount was adsorbed, TC in zwitterionic (TCH_2) form. Above pH 7, the surface charge of maghemite nanoparticles is negative, while

TC appears in mono (TC^-) and double anionic states (TC^{2-}), instead of electrostatic repulsion between the like-charges, close to 51 and 32 mg g^{-1} were adsorbed at pH 8 and 10, respectively. Based on this analysis, the adsorption of TC on maghemite nanoparticles did not occur through electrostatic interaction.

2.3. Adsorption Kinetics

The amount of TC that was adsorbed as a function of contact time was studied to establish the approximate equilibrium time. In this study, the dosage (10 mg) of MG was fixed and the pH was adjusted to optimum pH 6. As shown in Figure 4A, 15% of the initial concentration was adsorbed after 20 min of contact time. This increased steadily until 420 and 540 min, where equilibrium was reached with approximately 46% adsorption of the initial 50 mg L^{-1} initial concentration. At the equilibrium time, all the active sites have been occupied with the adsorbed TC molecules; therefore, furthering the contact will not bring any significant difference in the amount adsorbed. The data were further fitted into the linear form of pseudo-first and second-order kinetic models.

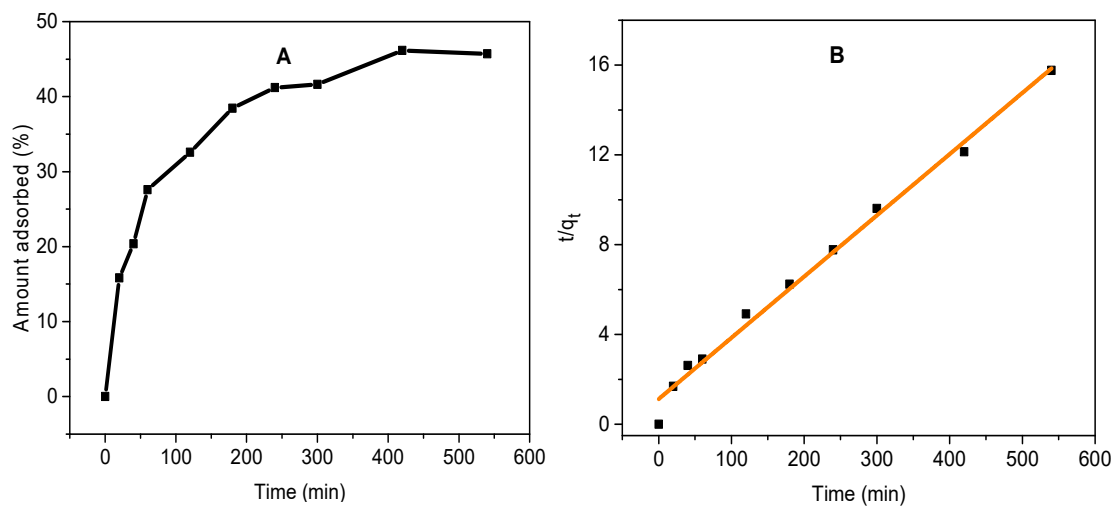


Figure 4. The effect of the amount of TC adsorbed as a function of contact time (A) and pseudo-second-order kinetic plot for the adsorption of TC (B).

The linear equation of pseudo-first and second order is given in Equations (2) and (3), respectively.

$$\log(q_e - q_t) = \log q_e - \frac{k_1 t}{2.303} \quad (2)$$

$$\frac{t}{q_t} = \frac{1}{k_2 q_e^2} + \frac{t}{q_e} \quad (3)$$

where q_e are adsorption capacity at equilibrium (mg g^{-1}), q_t is the amount of TC adsorbed at time t , k_1 is the rate constant of pseudo-first-order, k_2 is the rate constant of pseudo-second-order, and t is contact time (min).

The plot of t/q_t versus t in Figure 4B is the linear form of the pseudo-second-order kinetics. The plot of $\log(q_e - q_t)$ versus t is not linear (Figure not shown). Based on this, it implies that the kinetics of TC adsorption on the iron oxide nanoparticles is in conformation with the pseudo-second-order model, which indicates that the adsorption rate depends on the adsorption capacity of the adsorbent (maghemite), not on the concentration of the adsorbate [42]. The $R^2_{adjusted}$ and rate constant of the model are 0.989 and $1.009 \times 10^{-3} \text{ min g mg}^{-1}$.

2.4. Adsorption Isotherm

This study was done at optimum pH and time as earlier discussed. Non-linear forms of the two commonly used adsorption isotherms (Langmuir and Freundlich) were used to fit the experimental data obtained at various concentrations (20, 60, 100, 140, 160, 180 and 200 mg L⁻¹) of TC and constant amount of maghemite, and room temperature. The curve fit is shown in Figure 5. Equations (4) and (5) listed below define Langmuir and Freundlich isotherms, respectively.

$$q_e = \frac{q_{max}C_eK_L}{(1 + K_L C_g)} \quad (4)$$

$$q_e = K_F C_e^{1/n_F} \quad (5)$$

where C_e is the equilibrium concentration in solution (mg L⁻¹), q_e is the amount of TC that was adsorbed (mg g⁻¹), q_{max} is the maximum amount (mg g⁻¹) of adsorbed TC, K_L is Langmuir equilibrium constant (L mg⁻¹), K_F is the Freundlich constant (mg g⁻¹ (mg L⁻¹)^{-1/n_F}), n_F is the dimensionless exponent of Freundlich. The values of $R^2_{adjusted}$ obtained from the Langmuir and Freundlich nonlinear curve fit are 0.989 and 0.979, respectively, while the values of standard deviation are 2.91 and 4.02, respectively. This shows that our experimental data are best fitted into the isotherm according to the Langmuir model. Therefore, TC molecules were adsorbed on maghemite nanoparticles in a monolayer form without any interaction between the adsorbed molecules [43]. The monolayer adsorption capacity of maghemite nanoparticles for the adsorption of TC was found to be 97 mg g⁻¹. This value was compared with other adsorbents that were reported in the literature for the adsorption of TC. As listed in Table 1, our material (synthesized maghemite nanoparticles) performed better than some reported adsorbents.

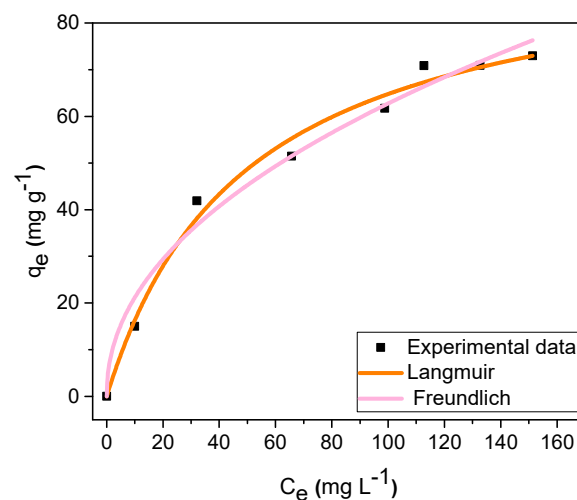


Figure 5. Adsorption isotherms for the removal of TC.

The results contained in Table 1 show that the use of maghemite nanoparticles for TC adsorption is very advantageous in light of their superparamagnetic properties. After the adsorption, they can be extracted from the solution with help of an external magnetic field, and, after removal/decomposition of contaminant, maghemite nanoparticles can be re-used for further decontamination. Moreover, since these nanoparticles present a semiconducting behavior, they can be used as photocatalysts for TC degradation, as discussed later in the text.

Table 1. Comparison of the maximum adsorption (q_{max}) of different adsorbents for the removal of TC.

Adsorbents	q_{max} (mg g ⁻¹)	References
Fe-doped zeolite	204	[44]
Fe ₃ O ₄ @C	14	[45]
Hydrous ferric oxide	41	[46]
Zn/Fe/La LDH	170	[47]
R600	14	[48]
Pistachio shell coated with ZnO	95	[49]
Cu-immobilized alginate	58	[50]
Magnetic porous carbon	25	[51]
Maghemite nanoparticles	97	This study

2.5. Proposed Mechanisms of TC Adsorption on Maghemite Nanoparticles

As discussed earlier, the adsorption of TC on the synthesized maghemite nanoparticles is not influenced by electrostatic interaction. To have a clue on the mechanism of adsorption, we examined the difference in the FTIR spectra of maghemite nanoparticles before and after the adsorption of TC. The obtained spectra, including the FTIR spectrum of TC, are presented in Figure 6A. The characteristic fingerprint of tetracycline could be found below 1700 cm⁻¹. Among these peaks the absorption band at 1611 cm⁻¹ is assigned to -COO-asymmetric vibration of TC. The -OH and -NH stretching of TC appeared at 3358 and 1575 cm⁻¹, respectively, while the aromatic in-plane and out-of-plane vibrations appeared at 1247–1000 cm⁻¹ and 567–501 cm⁻¹, respectively [47]. The peak at 3420 cm⁻¹ on the nanoparticle spectra is due to the presence of bulk -OH stretching [52]. While characteristic peak at 493 cm⁻¹ is due to the presence of Fe-O. After adsorption of TC, the intensity of the absorption band at 3420 cm⁻¹ increased, which is an indication of the hydrogen bond between the O atom of maghemite nanoparticles and the H atom of TC. This type of observation was also noticed by Tran et al. [53] in which there was a difference in the intensity of the -OH absorption band after removal of cationic dye on pristine biosorbent. The authors attributed this to the existence of both dipole-dipole and Yoshida hydrogen bonding interactions. Olusegun and Mohallem [54] also observed the same scenario in their study on the adsorption of doxycycline using kaolinite-supported CoFe₂O₄ nanoparticles. The peak attributed to the C=O group of TC at 1611 cm⁻¹ shifted to 1622 cm⁻¹ after the adsorption on nanoparticles. It could imply the *n*- π interaction between the O atom of maghemite nanoparticles and the π bond of TC [55]. The presence of new peaks (1382 and 1222 cm⁻¹) at the marked portion (which was expanded in Figure 6B) of the spectrum of maghemite nanoparticles + TC suggested successful adsorption of TC. The intensity of the Fe-O range of maghemite between 700 to 493 cm⁻¹ [56] increased after the adsorption of TC, as it can be seen clearly in Figure 6B, which probably could be due to interaction between maghemite and the aromatic ring of TC. Given this, the mechanism of tetracycline adsorption could be proposed as hydrogen bond and *n*- π interaction. The likely scheme of the mechanism is shown in Figure 7.

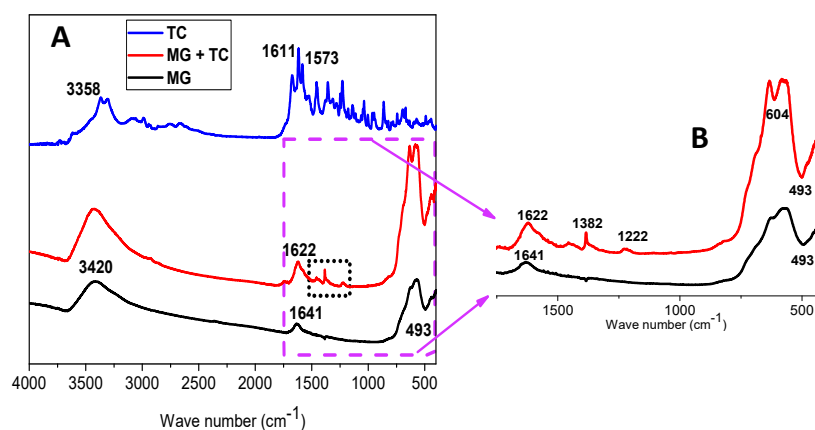


Figure 6. The FTIR spectra of maghemite before and after adsorption of tetracycline (4000–400 cm^{-1}) (A), and Enlarged portion of the maghemite spectra before and after adsorption of tetracycline (2000–400 cm^{-1}) (B).

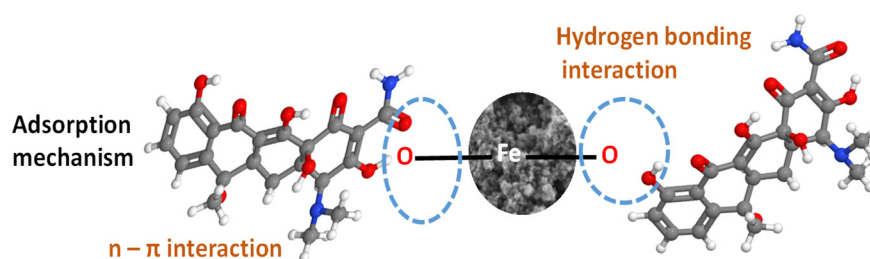


Figure 7. The likely mechanism of the adsorption of tetracycline on maghemite.

2.6. Photocatalytic Degradation of TC

The photocatalytic studies of maghemite nanoparticles were carried out after the adsorption equilibrium was reached (after 540 min interaction time) by degrading tetracycline under UV–vis light. To ensure that the result from the photocatalysis is not based on auto-photodegradation (photolysis), self-degradation of TC was carried out without the addition of maghemite nanoparticles. As shown in Figure 8A, TC in the absence of maghemite nanoparticles is relatively stable under UV/vis light (ca. 5% of the initial concentration degraded). However, when maghemite nanoparticles were added as the photocatalyst, TC became unstable, and approximately 40% of its initial concentration degraded after 60 min. We performed the same experiment for methylene blue (MB) photocatalytic degradation. In the case of MB, approximately 70% degraded in the presence of maghemite nanoparticles within 40 min of irradiation time already (Figure S2, supplementary Material). Since the amount of adsorbed TC is relatively high comparing some of the reported adsorbents (vide supra), therefore, we are inclined to assign this lower photodegradation of TC as compared to MB to the fact that the adsorbed TC molecules might screen the penetration of light from reaching the maghemite NPs surface. Thus, the generation of excited electrons and holes towards the photodegradation of TC was somehow impaired. For MB, where much more effective photodegradation was observed (see Supporting Information), no adsorption occurred within 24 h. Therefore, the penetration of photons into the maghemite was not hindered. This could as well explain the reason for the 70% degradation of its initial concentration within 40 min. Because of this, it could be affirmed that the adsorption of contaminants should be relatively moderate so that photocatalytic degradation would not be hindered. Additionally, one should also take into account that MB molecules absorbed light at a higher wavelength (665 nm), which required lower energy for its degradation compared to TC molecules that adsorbed light at a lower wavelength (345 and 270 nm) and therefore required higher energy for its degradation. It also shows that the bandgap of the synthesized maghemite nanoparticles is too narrow to prevent at least partial recom-

bination of photogenerated charges involved in TC degradation within the course of the experiment.

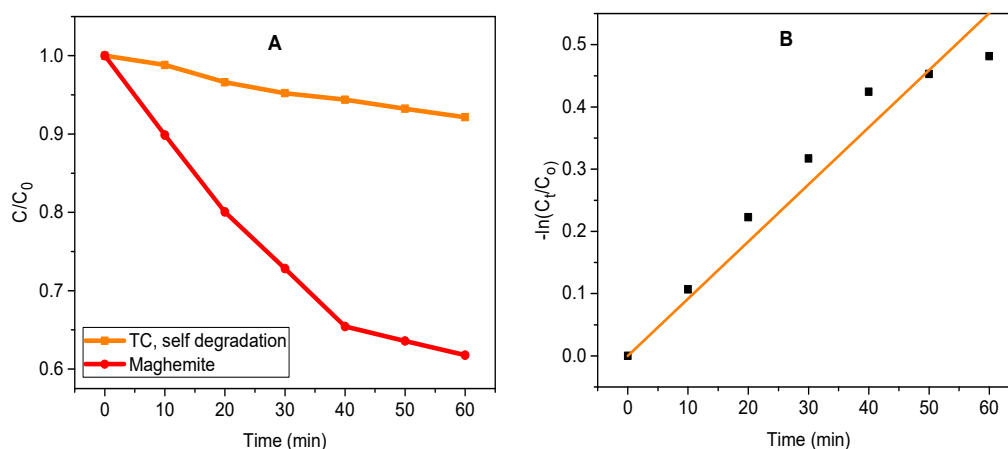


Figure 8. The concentration of TC with irradiation time in the presence and absence of maghemite nanoparticles (A) and pseudo-first-order kinetics (B) of TC in the time course of photodegradation.

The plot of $-\ln\left(\frac{C_t}{C_0}\right)$ versus t for pseudo-first-order is shown in Figure 8B. Here C_0 is the initial concentration ($83 \mu\text{M}$) of TC at time t is 0, and C_t stands for the TC concentration of sampling time in the course of photocatalysis. The adjustable correlation of coefficient ($R^2_{adjusted}$) is 0.98, while the rate constant is 0.0092 min^{-1} . Comparing the rate constant that we obtained with other published articles for the degradation of tetracycline, it is more than 0.003 min^{-1} that was obtained for $\alpha\text{-AgAl}_{0.4}\text{Ga}_{0.6}\text{O}_2$ [57] and 0.00599 min^{-1} that was reported for $0.3\text{-Au-TiO}_2/\text{PVDF}$ [58]. The assumption of this is that the rate of change of the solute uptake (in our case, tetracycline) with time is directly proportional to the difference in its saturation concentration on the surface of nanoparticles [42].

2.7. Proposed Mechanism of TC Photocatalytic Degradation

Prior to the explanation of the likely mechanisms, the band structure of maghemite nanoparticles was drawn based on the information from its bottom conduction band energy (E_{CB}) and bandgap energy (E_g) values. The value of the bottom of conduction band energy value (E_{CB}) can be estimated based on the energy corresponding to the flat band potential U_{fb} value of iron oxide nanoparticles, assuming their energies being equal: $E_{fb} \approx E_{CB}$. The flat band potential was determined through Mott–Schottky analysis [35] by extrapolating the linear portion of the inverse square of the capacitance of the space charge layer against the potential (Figure 9). The flat band potential extrapolated from the curve is -0.025 V vs $\text{Ag}/\text{AgCl}/3\text{M KCl}$ (pH 7), which is 0.172 V vs. SHE (standard hydrogen electrode) at pH 7. This value corresponds to the bottom of conduction band energy $E_{CB} = -4.67 \text{ eV}$. It is evident, in Figure 9, that the slope of the curve is positive implying that our maghemite is an n -type semiconductor. Recall that the evaluated maghemite nanoparticles' band gap value is 1.83 eV (*vide supra*); therefore, the value of top valence band energy (E_{VB}) is approximately 2.0 eV .

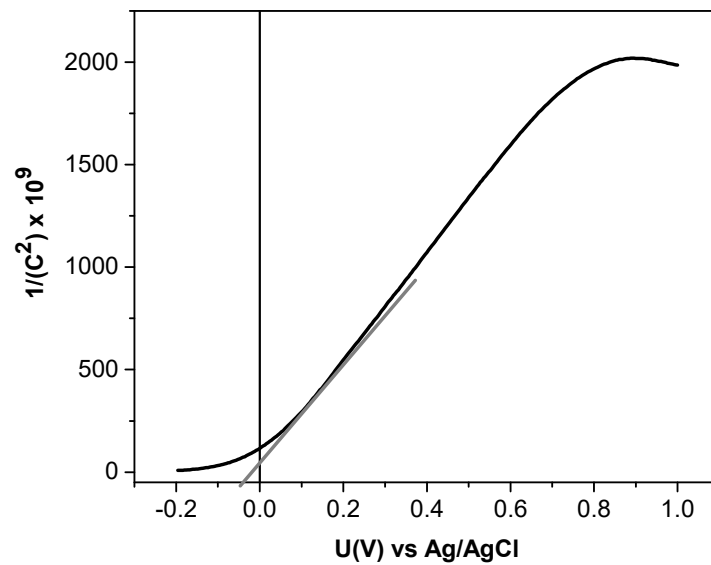


Figure 9. Mott–Schottky plot of maghemite nanoparticles.

The description of the mechanism of photocatalytic degradation of tetracycline by maghemite nanoparticles was based on the energy/potential diagram and the values of redox potential reactions, as shown in Figure 10.

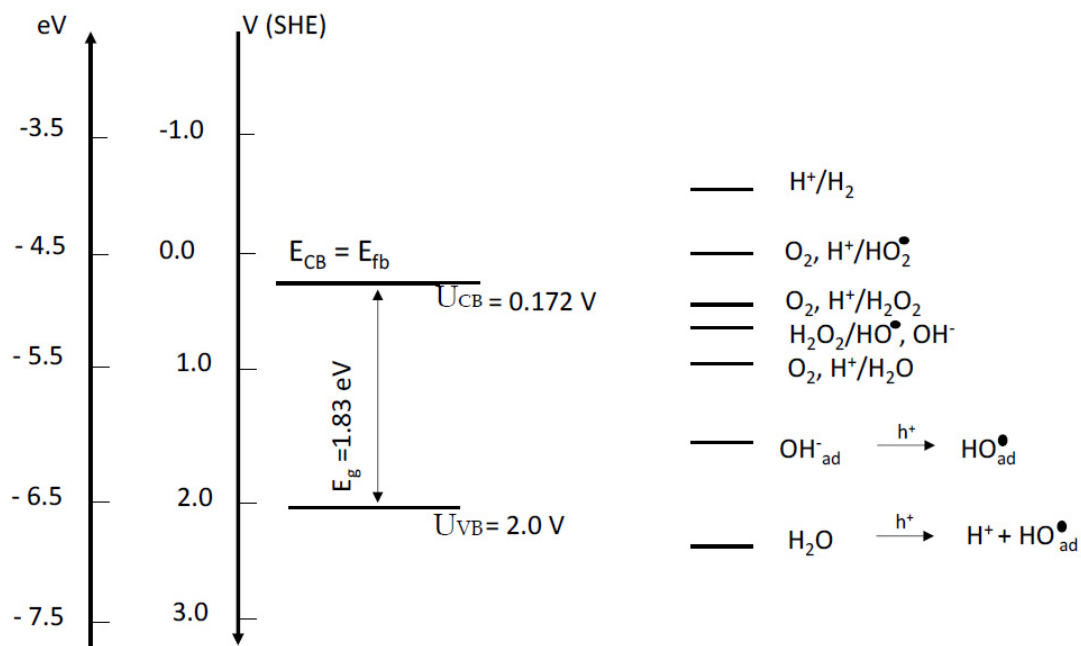


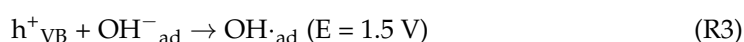
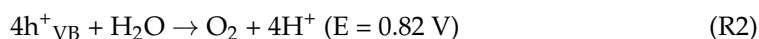
Figure 10. Schematic diagram of energy/potential diagram of maghemite nanoparticles and redox potential reactions of the photocatalytic degradation of tetracycline, pH 7.

As shown in Figure 10, the excited electrons from the valence band to the conduction band can reduce oxygen with the formation of H_2O_2 . This reaction can trigger additional reaction series—the photo-Fenton reaction [32]—and will be discussed below. Therefore, two mechanisms can be considered for the photocatalytic degradation of tetracycline on maghemite nanoparticles. In the first mechanism electrons and holes are generated in

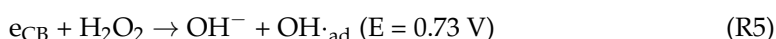
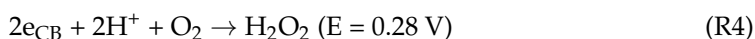
maghemite nanoparticles under illumination, reacting further with adsorbed TC, H_2O , OH^- , and oxygen in the solution. The pathways of these reactions can be as follows (pH 7):



for holes in the valence band



for electrons in the conduction band



These reactions are energetically favorable; however, the reaction (R3) is more probable than (R2), since only one hole is necessary for oxidation of adsorbed hydroxyl ion, instead of four in reaction (R2). The reactions (R3) and (R5) have been reported earlier [59,60]. Moreover, another reactions can take place in the iron oxide nanoparticles under illumination: reduction of ferric ions:



and oxidation of ferrous ions:



The standard potential of the $\text{Fe}^{3+}/\text{Fe}^{2+}$ redox couple is 0.77 V.

The hydroxyl radicals formed in reactions (R3) and (R5) are very reactive and can oxidize electron-rich organic molecules, like TC, and convert them to carbon dioxide and water (Figure 10, top pathway).



The second mechanism involved in the TC degradation can be directly related to the formation of H_2O_2 in the reaction (4) and with well-known photo-dissolution of iron oxides generating free Fe^{3+} and Fe^{2+} ions [61,62]. These ions appearing in the solution [32] together with H_2O_2 open up a new catalytic pathway: Fenton and photo-Fenton reactions, generating hydroxyl and hydroperoxyl radicals which can also participate in the degradation of tetracycline (Figure 11, top and bottom pathways):

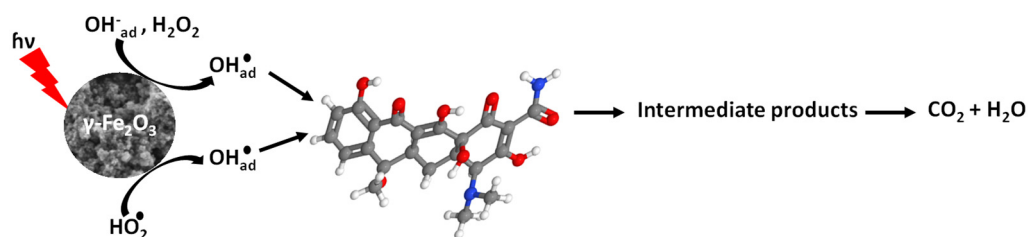


Figure 11. Photocatalytic degradation of tetracycline reaction with hydroxyl radicals.

Taking into account that during illumination of maghemite, the redox reaction (R6) and (R7) are possible, the Fenton reaction may be the heterogeneous one occurring also on the nanoparticle surface. In the course of the above reactions, the hydroxyl and hydroperoxyl radicals are being produced, entering also the degradation processes of tetracycline

(Figure 11, bottom pathway). Finally, the proposed scheme of catalytic photodegradation of TC is summarized in Figure 11, in which both photocatalytic pathways are presented graphically.

Recognizing also that during the illumination of maghemite, the redox reaction (R6) and (R7) are possible, the Fenton reaction may be the heterogeneous one occurring also on the nanoparticle surface. In the course of the above reactions, the hydroxyl and hydroperoxyl radicals are being produced, entering also the degradation processes of tetracycline (Figure 11, bottom pathway). Finally, the proposed scheme of catalytic photodegradation of TC is summarized in Figure 11, in which both photocatalytic pathways are presented graphically.

Our data presented in Figure 8 show that maghemite nanoparticles are less efficient as photocatalysts than other nanoparticulate semiconducting systems, such as metal oxides, mixed oxides, or CdS. In the case of these systems, 95% degradation was achieved within 60 min of the UV illumination [19,27,63,64].

However, there exists a substantial advantage of using maghemite in the environmental remediation studies, stemming from the fact that such “rust” particles showing superparamagnetic and photocatalytic properties are economically competitive to other nano adsorbents and nanocatalysts, due to the opportunity for magnetic separation and further reuse in combined adsorption and photocatalytic treatment of wastewater. Additionally, superparamagnetic iron oxide nanoparticles can open up a new photocatalytic photo-Fenton degradation pathway of persistent organic pollutants, increasing their efficiency in wastewater decontamination.

The pathway of TC photodegradation, shown in Figures 8 and 11, can proceed via initial TC oxidation by dominant radicals OH^\bullet , triggering a ring-opening reaction, and the detachment of acylamino and hydroxyl groups followed by further oxidation [65]. The observed decay of absorbance at 270 nm (Figure S3A, Supporting Information) can be related to the production of acylamino and hydroxyl groups and degradation of aromatic ring A, whereas simultaneous, gradual decrease of the absorption band at 360 nm can be related to degradation of aromatic ring B [63,66]. Alternative degradation pathways might exist, as noted in several publications [67,68].

The effect of hydroxyl radicals OH^\bullet in the photocatalytic action of maghemite nanoparticles was confirmed by the addition of isopropanol (100 mg/L)—well-known scavenger of OH^\bullet . The results, as shown in Figure S3B,C, show that isopropanol scavenged hydroxyl radicals, which resulted in the reduction of the rate of the degradation process. We also checked the effect of hydrogen peroxide that can be involved in Fenton and photo-Fenton reactions, by introducing H_2O_2 (100 mg/L) [65] into the reaction solution. This led to substantial increase in the rate of photocatalytic degradation of TC, Figure S3B,C. As shown in the pathway, the addition of H_2O_2 to the system resulted in the acceptance of the electron from the conduction band by H_2O_2 , thereby resulting in more production of hydroxyl radicals that speed up the photocatalytic degradation process. The rate constant decreased to 0.0046 min^{-1} when isopropanol was added, and increased to 0.0387 min^{-1} when H_2O_2 was introduced into the system, from its initial value of 0.0092 min^{-1} .

We are also aware that some of the intermediate compounds can be quite stable, as well as toxic [69,70]. At this point, we need to stress that our data show that the photodegradation of tetracycline, as proposed by Equation (8) and Figure 11, represents an ideal situation, yet as of now, apparently far from achieving total mineralization. On the contrary, it can proceed through various condition-dependent pathways with different efficiencies, as reported in the cited references.

3. Materials and Methods

3.1. Materials

Iron(II)chloride tetrahydrate ($\text{FeCl}_2 \cdot 4\text{H}_2\text{O}$), Iron(III)chloride hexahydrate ($\text{FeCl}_3 \cdot 6\text{H}_2\text{O}$), ammonium hydroxide (25% NH_3 , assay 99.99%), and tetracycline hydrochloride of analytical grade were purchased from Sigma-Aldrich (Poznan, Poland, Hydrogen peroxide

30% pure, p.a. was purchased from Chempur, Poland, 2-propanol (isopropanol) 99.7% was from POCH, Poland. All the chemicals were used without further purification.

Deionized water with a resistivity of 18.2 M Ω .cm obtained from the Milli-Q ultra-pure water filtering system from Merck (Darmstadt, Germany) was used throughout the experiment.

3.2. Synthesis of Superparamagnetic Maghemite Nanoparticles

Maghemite nanoparticles were synthesized by co-precipitation of FeCl₃·6H₂O and FeCl₂·4H₂O following the report of Rehman et al. [31]. In summary, 1.613 g of FeCl₃·6H₂O and 0.948 g of FeCl₂·4H₂O were dissolved in 22.25 mL of deionized H₂O with vigorously stirring at 75 °C. Once dissolved, 3.8 mL of ammonium hydroxide (ammonia 25%) was added to the solution. After 15 min of vigorous stirring, the solution is cooled, the supernatant was discarded and the precipitate formed was washed with deionized water several times until pH is approximately 7.

3.3. Characterization of the Synthesized Nanoparticles

Scanning electron microscope (SEM), Merlin, manufactured by Zeiss, Stuttgart, Germany, was used to examine the morphology of the synthesized iron oxides nanoparticles. Transmission electron microscopy (TEM) image was viewed on Zeiss Libra 120 Plus, Stuttgart, Germany, operating at 120 kV. Nanoparticle's solution was dropped on standard formvar-coated copper grids and air-dried overnight. Powder X-ray diffractograms were recorded with a diffractometer Bruker (Billerica, MA, USA), D8 Discover with Debye-Scherrer geometry at room temperature with a copper K α X-ray line $\lambda = 1.540598 \text{ \AA}$. Data were analyzed with DIFFRAC.EVA and TOPAS 4.2 programs. UV-vis absorption spectra of the nanoparticles were recorded using a Perkin Elmer Lambda 35 (Madison, WI, USA) to estimate the bandgap energy. FTIR spectra were recorded with ThermoFisher Scientific Nicolet 8700 spectrometer, Madison, WI, USA). The Malvern Zetasizer Nano ZS, Malvern, United Kingdom apparatus was used to evaluate the zeta potential of the nanoparticles. Magnetic characterization of powder samples was performed employing a vibrating sample magnetometer (VSM, Quantum Design, Darmstadt, Germany). Small amounts of samples (up to several milligrams) were placed in a plastic holder. The hysteresis loops were recorded varying the magnetic field between -2.0 and $+2.0$ T at temperature 300 K, stabilized with 0.01 K accuracy.

3.4. Evaluation of the Flat-Band Potential of Iron Oxide Nanoparticles

Alternate current (AC) voltammetry at 100 Hz (CH Instruments 660C) with a typical three-electrode system was used to evaluate the capacitance characteristics vs. polarization potential of the synthesized iron oxide nanoparticles. The out-of-phase current vs. potential curves were recorded with glassy carbon electrode (GCE) as working electrode with drop-cast iron oxide nanoparticles on its surface, Pt mesh as auxiliary, and Ag, AgCl | 3M KCl(aq) as the reference electrode. The obtained capacitances values were then used in the Mott-Schottky analysis to determine the value of the flat band potential and corresponding energy value (E_{fb}). In such analysis, the capacitance of an interface between semiconductor and electrolyte is equal to the semiconductor space-charge layer capacitance, C . This capacitance is related to the semiconductor flat band potential by the Mott-Schottky Equation (6):

$$\frac{1}{C^2} = \frac{2}{\epsilon\epsilon_0eN_d} \left(U - U_{fb} - \frac{k_B T}{e} \right) \quad (6)$$

where ϵ and ϵ_0 are the dielectric constant and the vacuum permittivity, respectively, e is the electronic charge, N_c is the charge carrier concentration, k_B is the Boltzmann constant, and T is the temperature [K]. Thus, a plot of C^{-2} versus applied potential U reveals U_{fb} as the linearly extrapolated intercept with the potential U axis. Then, this value can be correlated with the value of conduction band energy.

3.5. Adsorption Studies

In this study, 10 mg of maghemite nanoparticles were added to beakers that contained 15 mL of 100 mg L⁻¹ of tetracycline solutions. The pH of the suspension was adjusted to 2, 4, 6, 8, and 10 using dilute sodium hydroxide and hydrochloric acid. After 24 h, maghemite nanoparticles were separated from tetracycline (TC) solutions by applying an external magnet. The concentration of unadsorbed TC was determined by measuring the absorbance at 357 nm using a UV-vis spectrophotometer (UV-2400 series). The amount (q) of adsorbed TC (mg g⁻¹) was calculated using Equation (7).

$$q = \frac{(C_o - C_e)V}{m} \quad (7)$$

C_o and C_e in the equation stand for initial and final concentration (mg L⁻¹) of TC in the solution, respectively, m is the mass of maghemite nanoparticles (g) and V is the volume of TC solution.

3.6. Photocatalytic Degradation

In this case, 10 mg of the maghemite nanoparticles were added to 10 mL solutions of 83 µM of tetracycline. The solutions were stirred for 500 min at 600 rpm under dark until adsorption equilibrium was attained. Under a light experiment, the respective solutions of tetracycline were irradiated for 60 min by a 280 W UV/Vis mercury quartz lamp (PLK-5, Poland, emission spectrum ranging from 180 nm to 623 nm). The emission spectrum of mercury lamp used in the TC degradation experiments (provided by manufacturer) can be found in the Figure S1 of the supplementary material. The sample of the solutions was taken at a regular time interval, analyzed on a UV-vis spectrophotometer for change in concentration.

4. Conclusions

The study has clearly shown that maghemite can work as an adsorbent and photocatalyst to treat tetracycline-contaminated water. The synthesized iron oxide (maghemite) nanoparticles are superparamagnetic, whose morphology depicts the agglomeration of small particles. The effect of solution pH showed that the optimum adsorption occurred at pH 6, with an equilibrium time of 540 min. Based on the information from the surface charge of maghemite, ionization of tetracycline, and FTIR spectra before and after adsorption, the mechanism of adsorption is proposed to be hydrogen bonding and $n-\pi$ interactions. Monolayer maximum adsorption capacity was found to be 97 mg g⁻¹. The photodegradation mechanism can be through the reaction of TC with hydroxyl radicals formed in the photoreaction and photo-Fenton reaction. The rate constants for the adsorption and photodegradation are $1.0086 \times 10^{-3} \text{ min g mg}^{-1}$ and 0.00918 min^{-1} , respectively. Our studies revealed the potential of maghemite nanoparticles as adsorbent and photocatalyst, which is an advantage in waste-water treatment. Their superparamagnetic behaviour makes them economically competitive to other nanocatalysts due to the opportunity for magnetic separation and catalyst reuse in photocatalytic combined with photo-Fenton treatment of wastewater.

Supplementary Materials: The following are available online at <https://www.mdpi.com/article/10.3390/catal11101243/s1>, Figure S1: The emission spectrum of mercury lamp used in the TC degradation experiments (provided by manufacturer). Figure S2: Photocatalytic degradation of methylene blue in time of the UV-vis irradiation in the absence (top line) and presence (bottom line) of maghemite. Figure S3: UV spectra of TC with MG (A); effect of H₂O₂ and isopropanol of the photocatalytic degradation of TC using MG (B), and rate constant (C).

Author Contributions: Conceptualization: P.K., K.J. and S.J.O.; methodology, M.O. and S.J.O.; formal analysis: S.J.O., M.O. and K.J.; investigation: G.L. and S.J.O.; resources: P.K.; data curation: S.J.O., G.L., K.J. and P.K.; writing—original draft preparation, S.J.O.; writing—review and editing:

S.J.O. and P.K.; supervision: P.K. All authors have read and agreed to the published version of the manuscript.

Funding: This research received no external funding.

Acknowledgments: Sunday J. Olusegun with No PPN/U LM/2020/1/00051/DEC/01, would like to thank the Polish National Agency for Academic Exchange (NAWA) for their support.

Conflicts of Interest: The authors declare no conflict of interest.

References

1. Kumar, A.; Pal, D. Antibiotic resistance and wastewater: Correlation, impact and critical human health challenges. *J. Environ. Chem. Eng.* **2018**, *6*, 52–58. [[CrossRef](#)]
2. Liu, S.; Xu, W.-H.; Liu, Y.-G.; Tan, X.-F.; Zeng, G.-M.; Li, X.; Liang, J.; Zhou, Z.; Yan, Z.-L.; Cai, X.-X. Facile synthesis of Cu(II) impregnated biochar with enhanced adsorption activity for the removal of doxycycline hydrochloride from water. *Sci. Total Environ.* **2017**, *592*, 546–553. [[CrossRef](#)]
3. Zhang, Q.Q.; Ying, G.G.; Pan, C.G.; Liu, Y.S.; Zhao, J.L. Comprehensive evaluation of antibiotics emission and fate in the river basins of China: Source analysis, multimedia modeling, and linkage to bacterial resistance. *Environ. Sci. Technol.* **2015**, *49*, 6772–6782. [[CrossRef](#)]
4. Kümmerer, K. Antibiotics in the aquatic environment—A review—Part I. *Chemosphere* **2009**, *75*, 417–434. [[CrossRef](#)] [[PubMed](#)]
5. Alsager, O.A.; Alnajrani, M.N.; Abuelizz, H.A.; Aldaghmani, I.A. Removal of antibiotics from water and waste milk by ozonation: Kinetics, byproducts, and antimicrobial activity. *Ecotoxicol. Environ. Saf.* **2018**, *158*, 114–122. [[CrossRef](#)] [[PubMed](#)]
6. Meng, F.; Ma, W.; Wang, Y.; Zhu, Z.; Chen, Z.; Lu, G. A tribo-positive Fe@MoS₂ piezocatalyst for the durable degradation of tetracycline: Degradation mechanism and toxicity assessment. *Environ. Sci. Nano* **2020**, *7*, 1704–1718. [[CrossRef](#)]
7. Hang, T.T.M.; Vy, N.H.T.; Hanh, N.T.; Pham, T.-D.; Yen, L.T.H. Facile synthesis of copper tungstate (CuWO₄) for novel photocatalytic degradation of tetracycline under visible light. *Sustain. Chem. Pharm.* **2021**, *21*, 100407. [[CrossRef](#)]
8. Bagheri, S.; Termehyousefi, A.; Do, T.O. Photocatalytic pathway toward degradation of environmental pharmaceutical pollutants: Structure, kinetics and mechanism approach. *Catal. Sci. Technol.* **2017**, *7*, 4548–4569. [[CrossRef](#)]
9. Li, W.; Shi, C.; Yu, Y.; Ruan, Y.; Kong, D.; Lv, X.; Xu, P.; Awasthi, M.K.; Dong, M. Interrelationships between tetracyclines and nitrogen cycling processes mediated by microorganisms: A review. *Bioresour. Technol.* **2021**, *319*, 124036. [[CrossRef](#)]
10. Xu, D.; Xiao, Y.; Pan, H.; Mei, Y. Toxic effects of tetracycline and its degradation products on freshwater green algae. *Ecotoxicol. Environ. Saf.* **2019**, *174*, 43–47. [[CrossRef](#)]
11. Ai, Y.; Liu, Y.; Huo, Y.; Zhao, C.; Sun, L.; Han, B.; Cao, X.; Wang, X. Insights into the adsorption mechanism and dynamic behavior of tetracycline antibiotics on reduced graphene oxide (RGO) and graphene oxide (GO) materials. *Environ. Sci. Nano* **2019**, *6*, 3336–3348. [[CrossRef](#)]
12. Ebimieowei, E.; Ibemolagi, A. Antibiotics: Classification and mechanisms of action with emphasis on molecular perspectives. *Int. J. Appl. Microbiol. Biotechnol. Res.* **2016**, *4*, 90–101.
13. Hou, J.; Chen, Z.; Gao, J.; Xie, Y.; Li, L.; Qin, S.; Wang, Q.; Mao, D.; Luo, Y. Simultaneous removal of antibiotics and antibiotic resistance genes from pharmaceutical wastewater using the combinations of up-flow anaerobic sludge bed, anoxic-oxic tank, and advanced oxidation technologies. *Water Res.* **2019**, *159*, 511–520. [[CrossRef](#)] [[PubMed](#)]
14. Baran, W.; Adamek, E.; Jajko, M.; Sobczak, A. Removal of veterinary antibiotics from wastewater by electrocoagulation. *Chemosphere* **2018**, *194*, 381–389. [[CrossRef](#)] [[PubMed](#)]
15. Liang, C.; Wei, D.; Zhang, S.; Ren, Q.; Shi, J.; Liu, L. Removal of antibiotic resistance genes from swine wastewater by membrane filtration treatment. *Ecotoxicol. Environ. Saf.* **2021**, *210*, 111885. [[CrossRef](#)] [[PubMed](#)]
16. Alonso, J.J.S.; El Kori, N.; Melián-Martel, N.; Del Río-Gamero, B. Removal of ciprofloxacin from seawater by reverse osmosis. *J. Environ. Manag.* **2018**, *217*, 337–345. [[CrossRef](#)]
17. Chen, J.; Liu, Y.S.; Zhang, J.N.; Yang, Y.Q.; Hu, L.X.; Yang, Y.Y.; Zhao, J.L.; Chen, F.R.; Ying, G.G. Removal of antibiotics from piggery wastewater by biological aerated filter system: Treatment efficiency and biodegradation kinetics. *Bioresour. Technol.* **2017**, *238*, 70–77. [[CrossRef](#)] [[PubMed](#)]
18. Alnajrani, M.N.; Alsager, O.A. Removal of Antibiotics from Water by Polymer of Intrinsic Microporosity: Isotherms, Kinetics, Thermodynamics, and Adsorption Mechanism. *Sci. Rep.* **2020**, *10*, 794. [[CrossRef](#)]
19. Nagamine, M.; Osiat, M.; Jackowska, K.; Kryszynski, P.; Widera-Kalinowska, J. Tetracycline Photocatalytic Degradation under CdS Treatment. *J. Mar. Sci. Eng.* **2020**, *8*, 483. [[CrossRef](#)]
20. Li, X.; Yang, Z.; Hu, D.; Wang, A.; Chen, Y.; Huang, Y.; Zhang, M.; Yuan, H.; Yan, K. Bimetallic Fe_xMn_y catalysts derived from metal organic frameworks for efficient photocatalytic removal of quinolones without oxidant. *Environ. Sci. Nano* **2021**, *8*, 2595–2606. [[CrossRef](#)]
21. Minale, M.; Gu, Z.; Guadie, A.; Kabtamu, D.M.; Li, Y.; Wang, X. Application of graphene-based materials for removal of tetracyclines using adsorption and photocatalytic-degradation: A review. *J. Environ. Manag.* **2020**, *276*, 111310. [[CrossRef](#)] [[PubMed](#)]
22. Slokar, Y.M.; Le Marechal, A.M. Methods of decoloration of textile wastewaters. *Dye. Pigment.* **1998**, *37*, 335–356. [[CrossRef](#)]

23. Wen, M.; Li, G.; Liu, H.; Chen, J.; An, T.; Yamashita, H. Metal–organic framework-based nanomaterials for adsorption and photocatalytic degradation of gaseous pollutants: Recent progress and challenges. *Environ. Sci. Nano* **2019**, *6*, 1006–1025. [[CrossRef](#)]
24. Olusegun, S.J.; de Sousa Lima, L.F.; Mohallem, N.D.S. Enhancement of adsorption capacity of clay through spray drying and surface modification process for wastewater treatment. *Chem. Eng. J.* **2018**, *334*, 1719–1728. [[CrossRef](#)]
25. Zheng, X.; Li, Y.; Peng, H.; Huang, Z.; Wang, H.; Wen, J. Efficient solar-light photodegradation of tetracycline hydrochloride using BiVO₄/MoO₃ composites. *Colloids Surfaces A Physicochem. Eng. Asp.* **2021**, *621*, 126599. [[CrossRef](#)]
26. Wu, J.; Xue, S.; Bridges, D.; Yu, Y.; Zhang, L.; Pooran, J.; Hill, C.; Wu, J.; Hu, A. Fe-based ceramic nanocomposite membranes fabricated via e-spinning and vacuum filtration for Cd²⁺ ions removal. *Chemosphere* **2019**, *230*, 527–535. [[CrossRef](#)] [[PubMed](#)]
27. Cai, Z.; Song, Y.; Jin, X.; Wang, C.C.; Ji, H.; Liu, W.; Sun, X. Highly efficient AgBr/h-MoO₃ with charge separation tuning for photocatalytic degradation of trimethoprim: Mechanism insight and toxicity assessment. *Sci. Total Environ.* **2021**, *781*, 146754. [[CrossRef](#)]
28. Mahmood, A.; Zulfiqar, S.; Ali, S.; Ammara, U.; Mahmood, K.; Farrukh, M.A.; Saeed, Z.; Ibrahim, M. Novel Fe₂O₃-CuO-MoO₃ Magnetic Nanocomposite for Photocatalysis of Methylene Blue. *J. Supercond. Novel Magn.* **2021**, *34*, 1791–1799. [[CrossRef](#)]
29. Sunil, K.C.; Utsav, S.; Nairy, R.K.; Chethan, G.; Shenoy, S.P.; Mustak, M.S.; Yerol, N. Synthesis and characterization of Zn_{0.4}Co_{0.6}Fe₂O₄ superparamagnetic nanoparticles as a promising agent against proliferation of colorectal cancer cells. *Ceram. Int.* **2021**, *47*, 19026–19035. [[CrossRef](#)]
30. Fuentes-García, J.A.; Diaz-Cano, A.I.; Guillen-Cervantes, A.; Santoyo-Salazar, J. Magnetic domain interactions of Fe₃O₄ nanoparticles embedded in a SiO₂ matrix. *Sci. Rep.* **2018**, *8*, 2–11. [[CrossRef](#)]
31. Rehman, A.; Daud, A.; Warsi, M.F.; Shakir, I.; Agboola, P.O.; Sarwar, M.I.; Zulfiqar, S. Nanostructured maghemite and magnetite and their nanocomposites with graphene oxide for photocatalytic degradation of methylene blue. *Mater. Chem. Phys.* **2020**, *256*, 123752. [[CrossRef](#)]
32. Giannakis, S.; Liu, S.; Carratalà, A.; Rtimi, S.; Amiri, M.T.; Bensimon, M.; Pulgarin, C. Iron oxide-mediated semiconductor photocatalysis vs. heterogeneous photo-Fenton treatment of viruses in wastewater. Impact of the oxide particle size. *J. Hazard. Mater.* **2017**, *339*, 223–231. [[CrossRef](#)] [[PubMed](#)]
33. Radoń, A.; Drygała, A.; Hawełek, Ł.; Łukowiec, D. Structure and optical properties of Fe₃O₄ nanoparticles synthesized by co-precipitation method with different organic modifiers. *Mater. Charact.* **2017**, *131*, 148–156. [[CrossRef](#)]
34. Itoh, H.; Sugimoto, T. Systematic control of size, shape, structure, and magnetic properties of uniform magnetite and maghemite particles. *J. Colloid Interface Sci.* **2003**, *265*, 283–295. [[CrossRef](#)]
35. Papadas, I.T.; Galatopoulos, F.; Armatas, G.S.; Tessler, N.; Choulis, S.A. Nanoparticulate metal oxide top electrode interface modification improves the thermal stability of inverted perovskite photovoltaics. *Nanomaterials* **2019**, *9*, 1616. [[CrossRef](#)] [[PubMed](#)]
36. Rekorajska, A.; Cichowicz, G.; Cyranski, M.K.; Pękała, M.; Kryszynski, P. Synthesis and characterization of Gd³⁺- and Tb³⁺-doped iron oxide nanoparticles for possible endoradiotherapy and hyperthermia. *J. Magn. Magn. Mater.* **2019**, *479*, 50–58. [[CrossRef](#)]
37. Zuo, W.; Li, N.; Chen, B.; Zhang, C.; Li, Q.; Yan, M. Investigation of the deprotonation of tetracycline using differential absorbance spectra: A comparative experimental and DFT/TD-DFT study. *Sci. Total Environ.* **2020**, *726*, 138432. [[CrossRef](#)]
38. Hsu, L.C.; Liu, Y.T.; Syu, C.H.; Huang, M.H.; Tzou, Y.M.; Teah, H.Y. Adsorption of tetracycline on Fe (Hydr)oxides: Effects of pH and metal cation (Cu²⁺, Zn²⁺ and Al³⁺) addition in various molar ratios. *R. Soc. Open Sci.* **2018**, *5*, 171941. [[CrossRef](#)]
39. Rivera-Utrilla, J.; Gómez-Pacheco, C.V.; Sánchez-Polo, M.; López-Peñalver, J.J.; Ocampo-Pérez, R. Tetracycline removal from water by adsorption/bioadsorption on activated carbons and sludge-derived adsorbents. *J. Environ. Manag.* **2013**, *131*, 16–24. [[CrossRef](#)]
40. Boguslavsky, Y.; Margel, S. Synthesis and characterization of poly(divinylbenzene)-coated magnetic iron oxide nanoparticles as precursor for the formation of air-stable carbon-coated iron crystalline nanoparticles. *J. Colloid Interface Sci.* **2008**, *317*, 101–114. [[CrossRef](#)]
41. Watanabe, H.; Seto, J. The Point of Zero Charge and the Isoelectric Point of γ -Fe₂O₃ and α -Fe₂O₃. *Bull. Chem. Soc. Jpn.* **1986**, *59*, 2683–2687. [[CrossRef](#)]
42. Ranjan, T.S.; Prelot, B. Chapter 7—Adsorption processes for the removal of contaminants from wastewater: The perspective role of nanomaterials and nanotechnology. In *Nanomaterials for the Detection and Removal of Wastewater Pollutants*; Elsevier: Amsterdam, The Netherlands, 2020; pp. 161–222.
43. Olusegun, S.J.; Mohallem, N.D.S. Insight into the adsorption of doxycycline hydrochloride on different thermally treated hierarchical CoFe₂O₄/bio-silica nanocomposite. *J. Environ. Chem. Eng.* **2019**, *7*, 103442. [[CrossRef](#)]
44. Jannat Abadi, M.H.; Nouri, S.M.M.; Zhiani, R.; Heydarzadeh, H.D.; Motavalizadehkakhky, A. Removal of tetracycline from aqueous solution using Fe-doped zeolite. *Int. J. Ind. Chem.* **2019**, *10*, 291–300. [[CrossRef](#)]
45. Soares, V.; Grando, M.C.; Colpani, G.L.; Silva, L.L.; Maria, J.; Mello, M. De Obtaining of Fe₃O₄@C Core-Shell Nanoparticles as an Adsorbent of Tetracycline in Aqueous Solutions 2. Experimental Procedure. *Mater. Res.* **2019**, *22*, 1–11. [[CrossRef](#)]
46. Zang, J.; Wu, T.; Song, H.; Zhou, N.; Fan, S.; Xie, Z.; Tang, J. Removal of tetracycline by hydrous ferric oxide: Adsorption kinetics, isotherms, and mechanism. *Int. J. Environ. Res. Public Health* **2019**, *16*, 4580. [[CrossRef](#)]
47. Zaher, A.; Taha, M.; Mahmoud, R.K. Possible adsorption mechanisms of the removal of tetracycline from water by La-doped Zn-Fe-layered double hydroxide. *J. Mol. Liq.* **2021**, *322*, 114546. [[CrossRef](#)]

48. Wang, H.; Fang, C.; Wang, Q.; Chu, Y.; Song, Y.; Chen, Y.; Xue, X. Sorption of tetracycline on biochar derived from rice straw and swine manure. *RSC Adv.* **2018**, *8*, 16260–16268. [[CrossRef](#)]
49. Mohammed, A.A.; Kareem, S.L. Adsorption of tetracycline from wastewater by using Pistachio shell coated with ZnO nanoparticles: Equilibrium, kinetic and isotherm studies. *Alex. Eng. J.* **2019**, *58*, 917–928. [[CrossRef](#)]
50. Zhang, X.; Lin, X.; He, Y.; Chen, Y.; Luo, X.; Shang, R. Study on adsorption of tetracycline by Cu-immobilized alginate adsorbent from water environment. *Int. J. Biol. Macromol.* **2019**, *124*, 418–428. [[CrossRef](#)]
51. Zhu, X.; Liu, Y.; Qian, F.; Zhou, C.; Zhang, S.; Chen, J. Bioresource Technology Preparation of magnetic porous carbon from waste hydrochar by simultaneous activation and magnetization for tetracycline removal. *Bioresour. Technol.* **2014**, *154*, 209–214. [[CrossRef](#)] [[PubMed](#)]
52. Zhu, Y.; Yang, Q.; Lu, T.; Qi, W.; Zhang, H.; Wang, M.; Qi, Z.; Chen, W. Effect of phosphate on the adsorption of antibiotics onto iron oxide minerals: Comparison between tetracycline and ciprofloxacin. *Ecotoxicol. Environ. Saf.* **2020**, *205*, 111345. [[CrossRef](#)]
53. Tran, H.N.; You, S.J.; Nguyen, T.V.; Chao, H.P. Insight into the adsorption mechanism of cationic dye onto biosorbents derived from agricultural wastes. *Chem. Eng. Commun.* **2017**, *204*, 1020–1036. [[CrossRef](#)]
54. Olusegun, S.J.; Mohallem, N.D.S. Comparative adsorption mechanism of doxycycline and Congo red using synthesized kaolinite supported CoFe₂O₄ nanoparticles. *Environ. Pollut.* **2020**, *260*, 114019. [[CrossRef](#)]
55. Tran, H.N.; Wang, Y.F.; You, S.J.; Chao, H.P. Insights into the mechanism of cationic dye adsorption on activated charcoal: The importance of II–II interactions. *Process. Saf. Environ. Prot.* **2017**, *107*, 168–180. [[CrossRef](#)]
56. Cornell, R.M.; Schwertmann, U. *The Iron Oxides: Structure, Properties, Reactions, Occurrences and Uses*, 2nd ed.; Wiley-VCH Verlag GmbH & Co. KGaA: Weinheim, Germany, 2003.
57. Hou, X.; Wang, Z.; Chen, J.; Wang, J.; Lu, Q.; Wu, D. Facile construction of silver-based solid solution heterophase for efficient visible-light-driven photocatalytic degradation of tetracycline. *Chem. Eng. J.* **2021**, *414*, 128915. [[CrossRef](#)]
58. Yan, M.; Wu, Y.; Liu, X. Photocatalytic nanocomposite membranes for high-efficiency degradation of tetracycline under visible light: An imitated core-shell Au-TiO₂-based design. *J. Alloys Compd.* **2021**, *855*, 157548. [[CrossRef](#)]
59. Lawless, D.; Serpone, N.; Meisel, D. Role of hydroxyl radicals and trapped holes in photocatalysis. A pulse radiolysis study. *J. Phys. Chem.* **1991**, *95*, 5166–5170. [[CrossRef](#)]
60. Nosaka, Y.; Nosaka, A. Understanding Hydroxyl Radical (•OH) Generation Processes in Photocatalysis. *ACS Energy Lett.* **2016**, *1*, 356–359. [[CrossRef](#)]
61. Krýsa, J.; Jirkovský, J.; Bajt, O.; Mailhot, G. Competitive adsorption and photodegradation of salicylate and oxalate on goethite. *Catal. Today* **2011**, *161*, 221–227. [[CrossRef](#)]
62. Voelker, B.M.; Morel, F.O.M.M.; Sulzberger, B. Iron Redox Cycling in Surface Waters: Effects of Humic Substances and Light. *Environ. Sci. Technol.* **1997**, *31*, 1004–1011. [[CrossRef](#)]
63. Zhu, X.D.; Wang, Y.J.; Sun, R.J.; Zhou, D.M. Photocatalytic degradation of tetracycline in aqueous solution by nanosized TiO₂. *Chemosphere* **2013**, *92*, 925–932. [[CrossRef](#)]
64. Vasallo-Antonio, R.; Peña-Bahamonde, J.; Susman, M.D.; Ballesteros, F.C.; Rodrigues, D.F. Design and performance of Fe₃O₄@SiO₂/MoO₃/polydopamine-graphene oxide composites for visible light photocatalysis. *Emergent Mater.* **2021**, 1–15. [[CrossRef](#)]
65. López-Peñalver, J.J.; Sánchez-Polo, M.; Gómez-Pacheco, C.V.; Rivera-Utrilla, J. Photodegradation of tetracyclines in aqueous solution by using UV and UV/H₂O₂ oxidation processes. *J. Chem. Technol. Biotechnol.* **2010**, *85*, 1325–1333. [[CrossRef](#)]
66. Safari, G.H.; Hoseini, M.; Seyedsalehi, M.; Kamani, H.; Jaafari, J.; Mahvi, A.H. Photocatalytic degradation of tetracycline using nanosized titanium dioxide in aqueous solution. *Int. J. Environ. Sci. Technol.* **2015**, *12*, 603–616. [[CrossRef](#)]
67. Li, S.; Hu, J. Photolytic and photocatalytic degradation of tetracycline: Effect of humic acid on degradation kinetics and mechanisms. *J. Hazard. Mater.* **2016**, *318*, 134–144. [[CrossRef](#)]
68. Jeong, J.; Song, W.; Cooper, W.J.; Jung, J.; Greaves, J. Degradation of tetracycline antibiotics: Mechanisms and kinetic studies for advanced oxidation/reduction processes. *Chemosphere* **2010**, *78*, 533–540. [[CrossRef](#)] [[PubMed](#)]
69. Cao, H.L.; Cai, F.Y.; Yu, K.; Zhang, Y.Q.; Lü, J.; Cao, R. Photocatalytic Degradation of Tetracycline Antibiotics over CdS/Nitrogen-Doped-Carbon Composites Derived from in Situ Carbonization of Metal-Organic Frameworks. *ACS Sustain. Chem. Eng.* **2019**, *7*, 10847–10854. [[CrossRef](#)]
70. Zhao, T.; Zheng, M.; Fu, C.; Li, G.; Xiong, Y.; Qiu, W.; Zhang, T.; Zhang, J.; Zheng, C. Effect of low-level H₂O₂ and Fe(II) on the UV treatment of tetracycline antibiotics and the toxicity of reaction solutions to zebrafish embryos. *Chem. Eng. J.* **2020**, *394*, 125021. [[CrossRef](#)]